Research Square

Preprints are preliminary reports that have not undergone peer review.
They should not be considered conclusive, used to inform clinical practice,
or referenced by the media as validated information.

Smoke spread and visibility loss in an aircraft cabin: implications for evacuation and firefighting

Changyuan He
Civil Aviation Management Institute of China
Pei Wang
China Fire and Rescue Institute
Yanbo Yin
China Fire and Rescue Institute
Mengjie Liang
Sichuan Vocational College of Judicial Police
Gang Wang
wanggang@mail.bnu.edu.cn

Beijing Normal University

Article

Keywords: Aircraft cabin fire, Smoke transport, Visibility, Computational fluid dynamics, Evacuation guidance, Firefighting access

Posted Date: November 20th, 2026

DOI: https://doi.org/10.21203/rs.3.rs-11588619/v1

License: This work is licensed under a Creative Commons Attribution 4.0 International License.
Read Full License

Additional Declarations: No competing interests reported.

Smoke spread and visibility loss in an aircraft cabin: implications for evacuation and firefighting

Changyuan He[1,2], Pei Wang[3,4], Yanbo Yin[3], Mengjie Liang[5] and Gang Wang[4,*]

[1]Civil Aviation Management Institute of China, Beijing 100102, China

[2]Key Laboratory of UAV Emergency Rescue Technology, Ministry of Emergency Management, Beijing 102202, China

[3]China Fire and Rescue Institute, Beijing 102202, China

[4]School of Technology for Sustainability, Beijing Normal University, Zhuhai 519087, China

[5]Sichuan Vocational College of Judicial Police, Deyang 618000, China

*Correspondence: Gang Wang (wanggang@mail.bnu.edu.cn)

Abstract

Smoke obscuration affects visual orientation during aircraft-cabin evacuation and firefighting access. We analysed three Fire Dynamics Simulator calculations with front, middle and rear prescribed sources reaching 100 kW in a generic single-aisle cabin under common ventilation conditions. Temperature and soot-density fields were combined with records at seven aisle stations and three heights to examine smoke spread and reflecting-target visibility. Reduced visibility extended beyond the most strongly heated regions and varied with longitudinal position and height. At 1.7 m, seven, seven and four stations in the front, middle and rear cases recorded interval-mean visibility below a descriptive 10 m comparison level; at 2.1 m, all seven did so in each case. A lower-height station near the middle source reached 1.74 m. An independent historical Boeing 707 cargo comparison showed that replacing experimental endpoint samples with interval means increased optical root mean square error by 15.42% at fixed comparison labels. The results identify spatial optical conditions for assessing evacuation wayfinding and firefighter orientation alongside thermal and gas conditions.

Keywords: Aircraft cabin fire; Smoke transport; Visibility; Computational fluid dynamics; Evacuation guidance; Firefighting access

Introduction

Smoke obscuration changes the visual information available to passengers and firefighters in an aircraft. Passengers need to follow aisle features and locate exit guidance, while firefighters need to identify the source and maintain their orientation during an approach. These tasks take place within a spatially varying thermal and gaseous environment. Aircraft fire assessment therefore benefits from describing where smoke accumulates, which parts of the occupied space lose visibility and how those regions relate to heating. Figure 1 places these observation needs in their aircraft and compartment context.

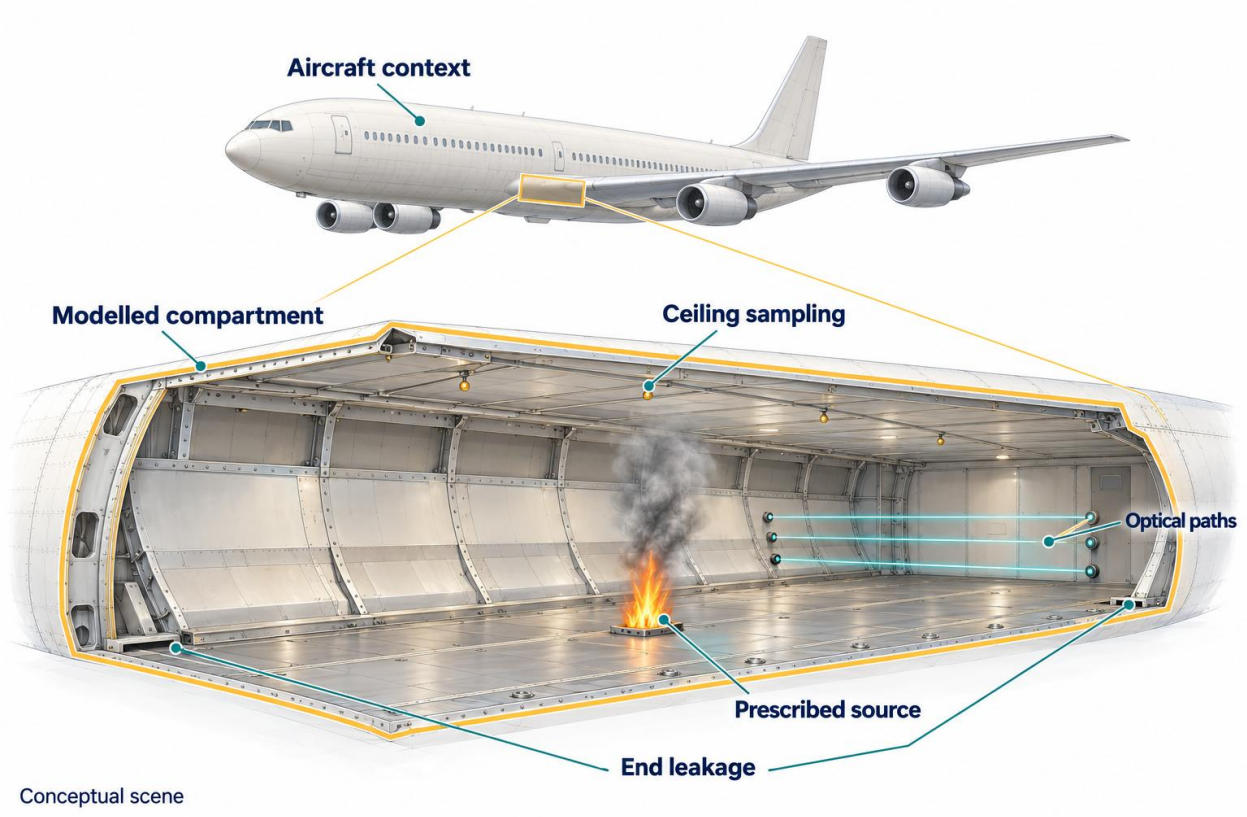


Figure 1. Aircraft context and lower-compartment observation schematic. The floor source, ceiling sampling, optical paths and end openings illustrate the historical cargo comparison. The passenger-cabin computational geometry and aisle observation coordinates are shown in Fig. 2.

Visibility is a connection between the fire environment and a particular visual task. Experiments on self-illuminated signs showed that readability through smoke depended on sign size and background luminance [1]. In a cabin, the smoke distribution also places the target and the observer within a confined longitudinal space. A useful environmental description identifies the conditions along that space, including the height at which visual information is assessed. This provides a basis for discussing exit guidance and firefighter orientation in terms of the locations and viewing conditions relevant to each task.

Fire calculations provide fields that can be examined at these locations. In Fire Dynamics Simulator (FDS), soot concentration is related to the light-extinction coefficient, from which visibility is estimated using a target-dependent factor [2]. The mass-specific extinction coefficient describes the optical properties assigned to the smoke [3], whereas the visibility factor represents the assumed visual target. Photometric studies of large fires further show the importance of the viewing path and measurement conditions [4]. These relationships tie the optical descriptor to the underlying soot field and the target definition.

Aircraft cargo research provides an established foundation for analysing evolving fire signatures. Previous work has compared smoke-transport calculations with experiments, examined ventilation effects and considered detector placement [5,6,7,8]. Actual and surrogate smoke can produce different early optical responses [9]. The historical FAA Boeing 707 dataset supplies thermal, optical and gas records from a common compartment experiment [10]. Together, these studies show the value of retaining source characteristics, transport conditions and observation definitions when interpreting a calculated fire environment. They also provide the context for examining the temporal basis of a numerical comparison.

Passenger-cabin interpretation adds an explicit spatial requirement. A source is located relative to the aisle, seating banks, overhead obstructions and imposed airflow. Moving that source changes its relationship to both the enclosure and the observation stations. Temperature and visibility can consequently describe different parts of the resulting environment. For evacuation wayfinding and firefighting access, the pertinent question concerns the distribution of these quantities along the cabin and between observation heights. A spatial comparison can identify which locations should be examined jointly when visual orientation and approach conditions are considered.

An aisle-based assessment asks whether obscuration is concentrated near the source or extends along the direction of movement. It also asks how the conditions at a selected height relate to the upper smoke region and to source-adjacent heating. These questions connect the shape of a field with the sampling layout used to describe it. A minimum visibility value identifies a pronounced local condition, while a station profile identifies where comparable conditions occur. Following those records through time adds the evolution needed to place a snapshot in context. This combination is useful when specifying an assessment of guidance features, a firefighter viewing position or an approach through the cabin. The spatial information supplies a common environmental basis for comparing such tasks at explicitly defined coordinates.

Time is equally important when the calculated fields are related to observations. Field snapshots, saved device means and experimental samples represent distinct forms of a transient record. Comparing them involves a choice of sampling labels and temporal support. The same physical calculation can therefore yield different error summaries when those choices change. An explicit comparison at common labels provides a way to examine the contribution of experimental

averaging while preserving the numerical records. This question is particularly relevant to smoke attenuation because its optical representation includes a nonlinear transformation.

The primary question in this study is how longitudinal source position and sampling height affect smoke obscuration relative to heating in a generic single-aisle cabin. We examined three prescribed-source calculations with common geometry and ventilation, using native soot-density and temperature fields together with aisle point histories. A second analysis used the historical B707 cargo case to examine thermal and optical discrepancies under three temporal comparisons. These two analyses retain the spatial and observational coordinates needed to interpret the results: position and height for the cabin, and quantity, channel and temporal support for the historical comparison.

The article first follows the cabin plume and compares the thermal and optical fields. It then examines visibility across seven aisle stations and three heights, alongside temperature and carbon monoxide. The historical analysis evaluates channel errors, recorded gas events and the response of error summaries to temporal pairing. The discussion connects these findings to evacuation guidance, firefighter orientation and the design of fire-protection assessments. Figure 2 defines the common passenger-cabin setting and the source and sampling coordinates used throughout the spatial comparison.

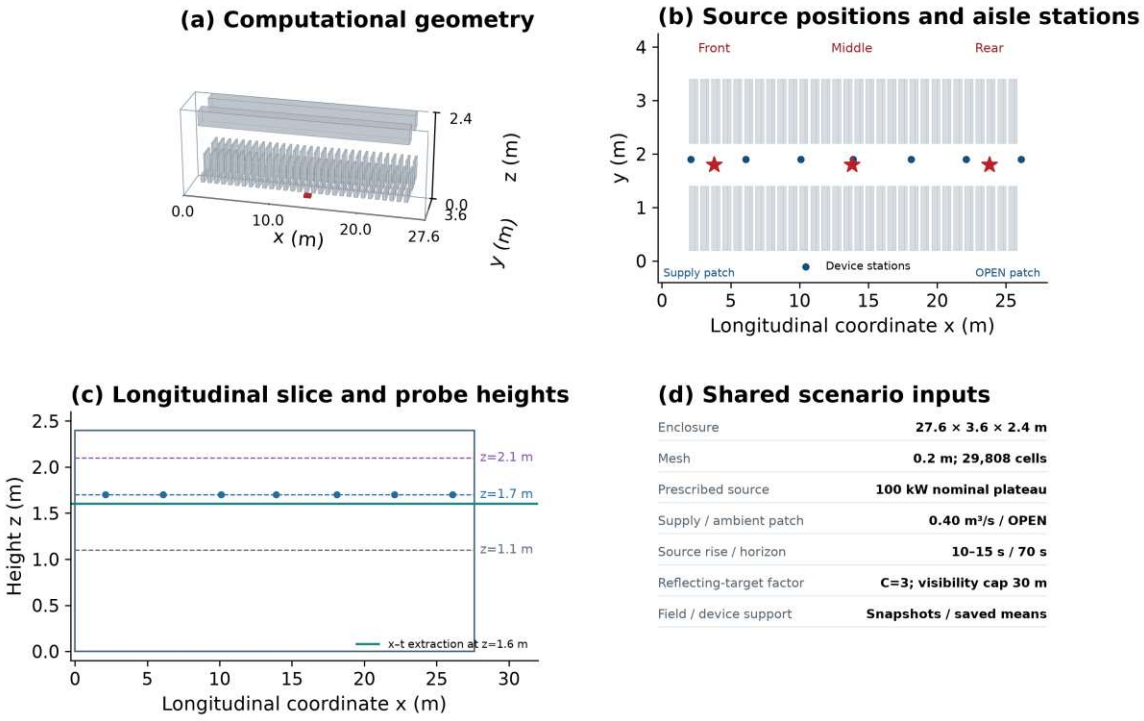


Figure 2. Generic single-aisle cabin and observation coordinates. (a) Seating-bank and overhead-bin proxies reconstructed from the initialized obstacle indices; the displayed box aspect is 27.6:5.5:10.5. (b) Front, middle and rear source centres and seven aisle stations. (c) Device heights and the z = 1.6 m node used for longitudinal space–time extraction. (d) Common model inputs. Coordinates and obstacle dimensions are specified in Methods.

Results

Smoke obscuration extended beyond the strongest heating

The middle-source sequence progressed from the prescribed non-burning startup to plume formation and smoke transport beneath the ceiling (Fig. 3). The first frame established the seating and overhead-bin geometry before the source developed. At 20.02 s, the rendered field located smoke above the source, and the later frames showed an elongated upper smoke region. The fixed view made these successive states directly comparable within the same cabin. It also retained the aisle as a common spatial reference for reading the plume and the upper accumulation.

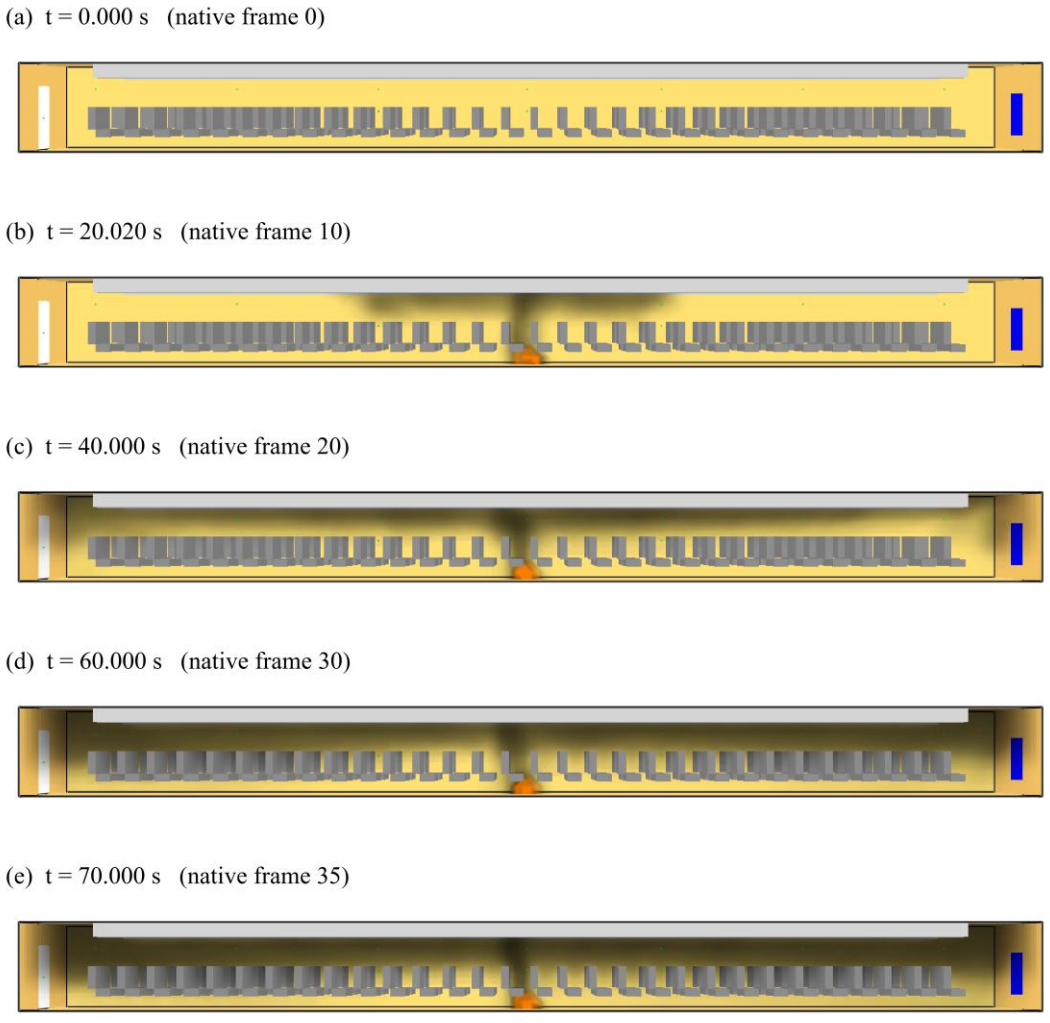


Figure 3. Smoke and fire evolution in the middle-source case. Smokeview images use the saved soot-density and heat-release fields at 0, 20.02, 40, 60 and 70 s. The fixed view places the supply patch on the right (x = 0) and the ambient OPEN patch on the left (x = 27.6 m). Panel labels identify physical times and saved frames.

At 70 s, the temperature and reflecting-target visibility maps described different spatial extents (Fig. 4). The strongest heating was concentrated near each source, whereas reduced visibility occupied a broader upper region. Common scales for each quantity made the three cases comparable. The contrast was visible within each source-position case, linking a local region of intense heating to a more extended region of optical attenuation. The calculated fields thus supplied two complementary descriptions of the same evolving fire environment.

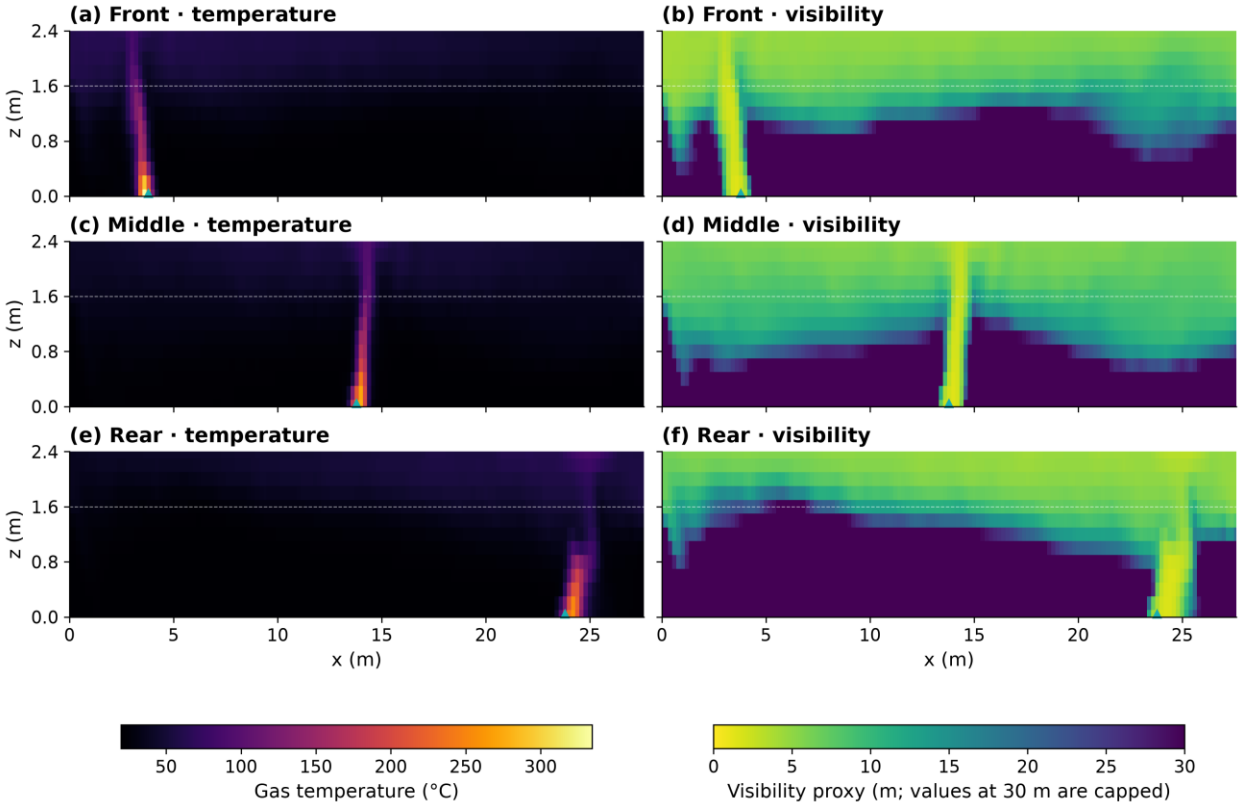


Figure 4. Longitudinal gas temperature and reflecting-target visibility at y = 1.8 m and 70 s for the three source positions. Each quantity uses a common scale across cases. Visibility is $S = \min(30\ \text{m}, 3/K)$, with $K = 8700\rho_s$. Cyan markers identify source locations; dashed lines mark z = 1.6 m.

Source position changed the longitudinal distribution under the common supply and ambient-opening arrangement. In the front-source case, the reduced-visibility region developed along increasing x, while the rear-source case retained a different longitudinal pattern (Fig. 5). The horizontal slices located these differences across the aisle plane, and the space–time maps retained their development along the cabin. Viewing the two representations together related the state at 70 s to the preceding evolution at the selected extraction height.

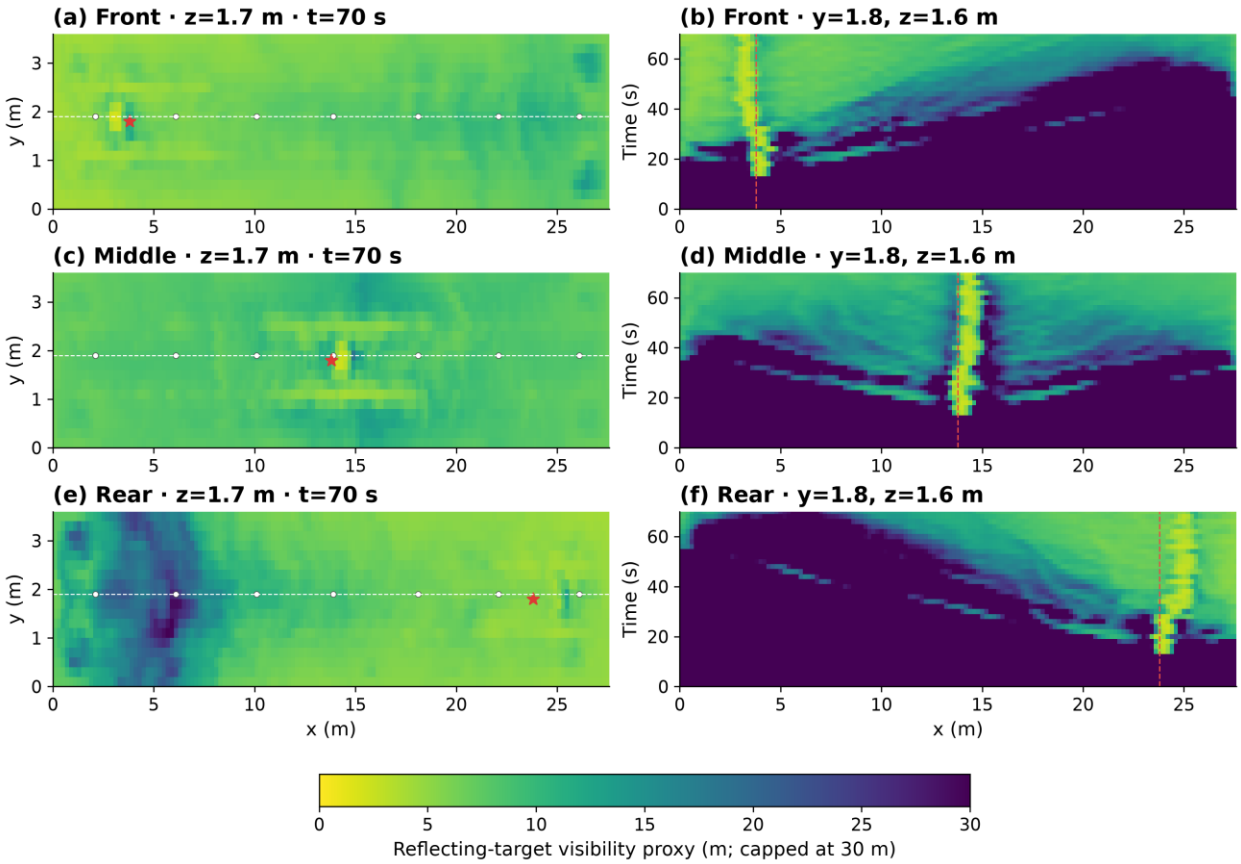


Figure 5. Spatial and temporal visibility on a common scale. Left: cell-centred horizontal slices at z = 1.7 m and 70 s, with device positions at y = 1.9 m and red stars identifying source centres. Right: longitudinal space–time maps at y = 1.8 m and z = 1.6 m; dashed vertical lines identify source centres. Solids are masked.

The spatial representations also connected the source location with the monitoring layout. Each case retained the same seven longitudinal stations, while the source centre moved from the front to the middle or rear. The maps therefore showed where the sampled stations lay relative to the evolving smoke region. This common coordinate system supported comparison of the station records with the longitudinal and horizontal fields. The field and device results together described how optical conditions varied within the represented cabin.

Aisle visibility varied with longitudinal position and height

The device summaries showed a pronounced height dependence (Fig. 6; Table 1). At z = 1.7 m, all seven stations in the front and middle cases and four stations in the rear case had at least one recorded interval mean below the descriptive 10 m comparison level. At z = 2.1 m, all seven stations did so in every case. At z = 1.1 m, the front and rear records remained above this level at every sampled station, with minimum values of 14.69 and 14.86 m. Upper attenuation was therefore more widespread than lower-height attenuation in those two cases.

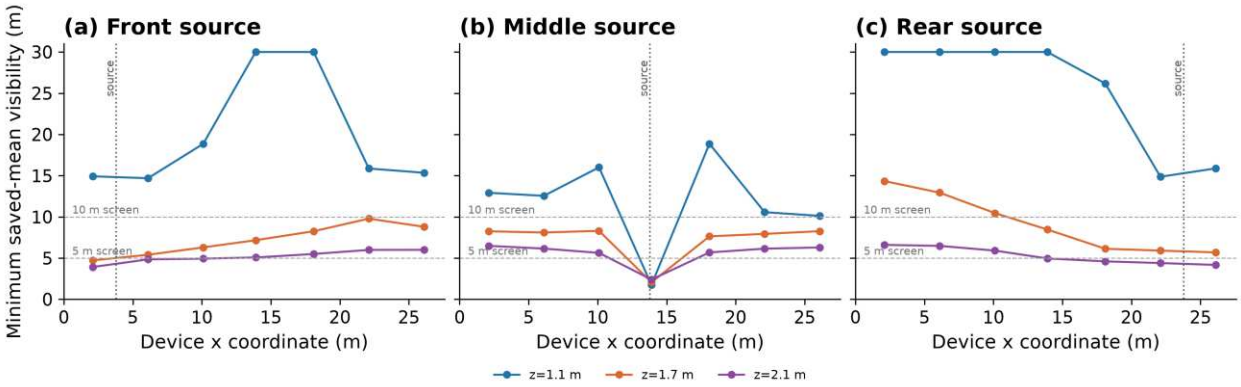


Figure 6. Minimum recorded interval-mean visibility over 0–70 s at seven aisle stations (y = 1.9 m) and three heights. Markers show station summaries and connecting lines aid comparison. Vertical dotted lines locate source centres. Horizontal lines identify the descriptive 5 and 10 m comparison levels.

Table 1. Cabin summaries across seven stations at each height, using recorded interval means after the initial record over 0–70 s.

Source	Height (m)	Min S(m)	Max T(°C)	Max CO(ppm)	N<10 m	N<5 m
Front	1.1	14.69	31.69	4.18	0	0
Front	1.7	4.72	56.84	14.12	7	1
Front	2.1	3.92	66.86	17.55	7	3
Middle	1.1	1.74	184.35	54.66	1	1
Middle	1.7	2.05	132.00	39.96	7	1
Middle	2.1	2.39	109.46	32.31	7	1
Rear	1.1	14.86	31.58	4.13	0	0
Rear	1.7	5.69	50.96	11.51	4	0
Rear	2.1	4.17	64.88	16.43	7	4

S denotes reflecting-target visibility. Minimum S, maximum temperature and maximum CO were computed independently over stations and time. Counts identify stations with at least one interval mean below the stated comparison level, among seven stations at each height.

The two comparison levels distinguished the distribution of moderate and stronger attenuation in the saved records. At 1.7 m, the front and middle cases each had one station below 5 m, while the rear case had zero. At 2.1 m, the corresponding counts were three, one and four stations. All three cases therefore shared seven stations below 10 m at the upper height, while the number below 5 m varied. This combination of counts retained information that a single minimum or a single comparison level would condense.

Minimum visibility also varied within the upper-height summaries. At 2.1 m, the front, middle and rear values were 3.92, 2.39 and 4.17 m, respectively. The separate maximum temperatures at that height were 66.86, 109.46 and 64.88 °C, with maximum CO values of 17.55, 32.31 and 16.43 ppm. These quantities were calculated across the same station sets, using independent extrema over the observation period. Table 1 preserves their physical units and the associated station counts for direct comparison between heights.

The middle-source case contained a localized departure from the comparatively clear lower-height pattern. At x = 13.9 m and z = 1.1 m, minimum recorded visibility was 1.74 m. The separate maximum temperature and CO values at that station were 184.35 °C and 54.66 ppm. Each value summarised a distinct extremum of the station record. The source centre was at x = 13.8 m, giving a longitudinal offset of 0.1 m; the nearest front- and rear-case stations were 1.7 m from their source centres. The coordinates locate the strongly obscured lower-height record immediately adjacent to the middle source.

At 1.7 m, the minimum visibility values across the seven stations were 4.72, 2.05 and 5.69 m for front, middle and rear sources. The corresponding maximum temperatures were 56.84, 132.00 and 50.96 °C, and maximum CO values were 14.12, 39.96 and 11.51 ppm. Comparing these summaries with the 1.1 and 2.1 m results shows that height influenced each environmental descriptor. The largest middle-case thermal excursion occurred in the lower, source-adjacent record, while the station counts showed widespread upper optical attenuation.

Temporal pairing changed optical and thermal error summaries differently

The historical B707 analysis compared the same numerical calculation using three temporal definitions. Protocol P used 181 experimental labels, while L and W used the same 36 nonzero native simulation labels and stored values. W replaced the experimental endpoint values used by L with preceding-interval means. This fixed-label comparison isolated the effect of changing experimental temporal support. The P and L comparisons additionally described the effect of sampling the residual histories on different grids.

Pooled thermocouple-rise RMSE was 1.357 K under P, 1.376 K under L and 1.378 K under W. Corresponding transmission RMSEs were 5.812, 5.935 and 6.850 percentage points in the metre-normalised quantity. P to L increased thermal and optical RMSE by 1.43% and 2.12%. At fixed native labels, L to W increased them by 0.13% and 15.42%. The combined P to W increases were 1.56% and 17.87%. These relative changes were obtained from the unrounded summaries, while the reported absolute errors are rounded to three decimals.

Mean absolute error and bias provided additional views of this change. Thermal MAE decreased from 1.139 K under L to 1.128 K under W, while thermal bias increased from +0.560 to +0.668 K. Optical bias changed from −4.046 to −4.881 points, and optical MAE increased from 4.409 to 5.104 points. Under P, thermal MAE and bias were 1.113 and +0.543 K, while optical MAE and

bias were 4.295 and −3.953 points. The comparison therefore retained both the magnitude and direction of the discrepancies.

Every channel retained its mean-bias sign across P, L and W (Fig. 7). Thirty-four thermocouple channels were positive, the same six were negative, and all six optical channels were negative. W increased RMSE relative to L in 28 of 40 thermocouple channels and every optical channel. Duration-weighted L and W RMSEs rounded to the same three-decimal values as their equally weighted counterparts. Optical duration-weighted MAE under L was 4.408 points, compared with 4.409 points using equal weights. The narrow interval-length range was therefore reflected in closely matching weighted summaries.

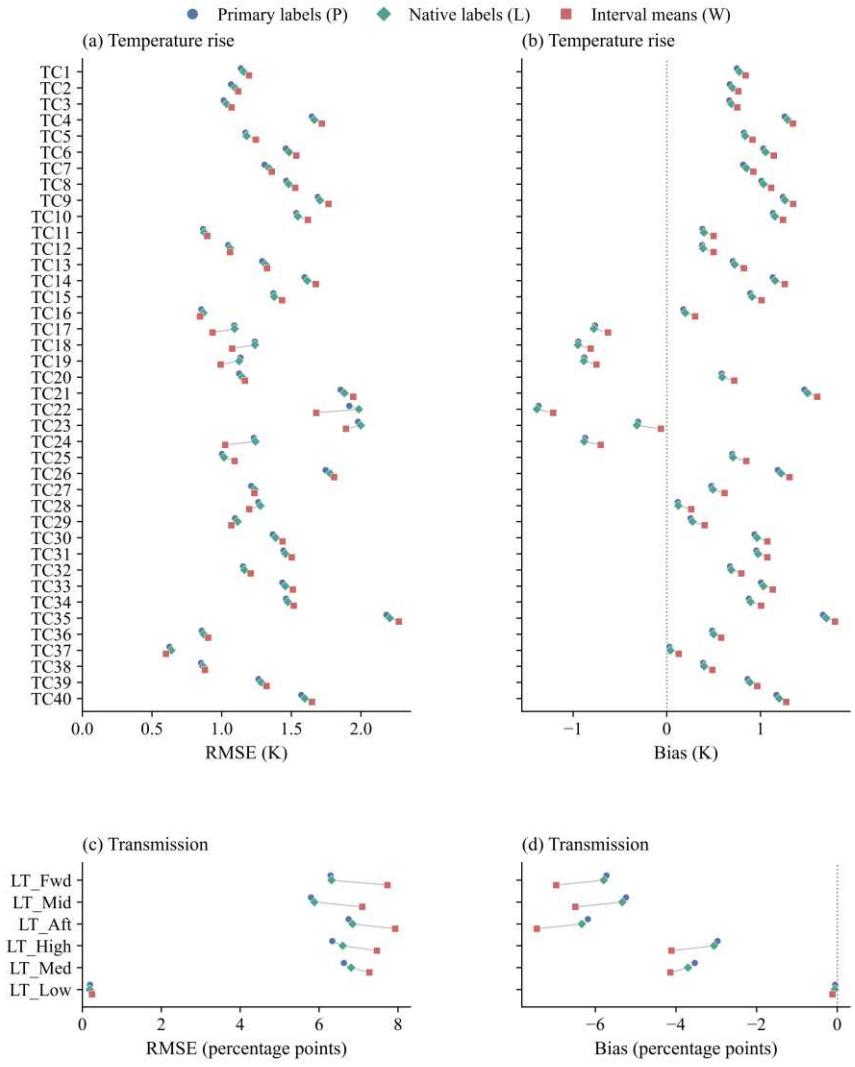


Figure 7. Channel RMSE and simulation-minus-experiment bias under P, L and W. P uses 181 experimental labels; L and W use 36 native labels with identical saved simulation values and weights. Connecting segments identify each channel across comparisons. Optical errors are percentage-point differences in metre-normalised transmission. All 40 thermocouple and six transmission channels are included.

Historical discrepancies depended on observation location and quantity

Thermocouple errors varied across the ceiling array. Under P, channel RMSE ranged from 0.625 K at TC37 to 2.182 K at TC35, with a median of 1.263 K. The six negative-bias channels were TC17, TC18, TC19, TC22, TC23 and TC24. Positive pooled thermal bias therefore coexisted with a spatial group of underpredicted records. The full set of channel summaries in Fig. 7 retained this distribution while also showing how each channel responded to the temporal comparison.

The largest whole-series error and largest individual thermal residual occurred at different channels. The largest absolute P pointwise residual was +4.305 K at TC23 and 86 s, whereas the largest channel RMSE occurred at TC35. At TC23, paired-grid maxima were 25.535 K at 90 s for the simulation and 23.21 K at 100 s for the experiment. These records distinguished the timing and magnitude of a local excursion from the error accumulated across a complete channel history.

Transmission RMSE ranged from 0.188 points at LT_Low to 6.748 points at LT_Aft, with a median of 6.310 points. LT_Low remained mostly clear in the experiment, with a minimum of 95.8%/m. The largest absolute paired optical residual was −20.517 points at LT_High and 80 s. The optical channels consequently covered different attenuation regimes and different combinations of local excursion and whole-history discrepancy. Their consistently negative mean biases corresponded to stronger predicted attenuation across all six paths.

For the 19 optical events explicitly tabulated in the FAA report, RMSE was 1.872 percentage points and MAE was 1.137 points in the original 0.3048 m reference-length convention. Signed residuals ranged from −5.431 to +1.693 points. These event errors described the report’s selected channel–time combinations, while the complete-series errors described all paired samples through 180 s in the metre convention. Both summaries retained their specified reference length and observation set.

The gas comparison comprised 18 printed records, including two TC36 entries at 60 s with inconsistent source-table values. Sixteen events supported interval judgements. All eight unambiguous CO predictions exceeded the corresponding reported upper uncertainty bounds. At 120 s, Mid Pan CO was 221.11 ppm, compared with 110.3 ± 25.6 ppm and an upper bound of 135.9 ppm. All six Mid and Aft CO_2 events fell within their printed intervals, while TC36 CO_2 at 120 and 180 s exceeded the respective upper bounds. These outcomes retained the differences between species and observation locations.

Early partition sensitivity at unchanged resolution

The historical five- and eight-mesh calculations were compared over their common 0–45 s interval. Median channel RMSE between them was 0.04794 K for thermocouple rise and 0.38536 transmission points. Maximum channel RMSEs were 0.36616 K at TC23 and 0.83556

points at LT_Mid. Maximum absolute paired differences were 1.05792 K at TC24 and 2.30727 points at LT_Fwd. The comparison retained all 46 principal channels on the common integer-second grid.

Heat-release RMSE between the two partitions was 0.0003793 kW, with a maximum absolute difference of 0.0016987 kW. In the 180 s calculation, the maximum stored heat-release interval mean was 4.2823 kW at 85.004 s. These quantities documented the source response and the early sensitivity to additional mesh interfaces. Together with the channel comparisons, they characterised the numerical histories produced by repartitioning the same initialized geometry and source faces.

Discussion

The cabin calculations show why smoke obscuration deserves an explicit spatial description in aircraft fire assessment. The region of strongest heating and the region of reduced visibility occupied different extents, and their relationship varied along the cabin and between sampling heights. For evacuation guidance and firefighting access, this means that locating the hottest region addresses one part of the environmental problem, while locating obscured visual cues addresses another. The useful result is the connection between calculated fields and the coordinates at which a particular movement or observation task takes place.

The combined use of fields and station histories makes that connection more informative. The longitudinal and horizontal maps retain the shape and extent of the smoke region, while the point records provide a common set of heights and stations for comparing quantities through time. Read together, these representations help identify locations for more detailed viewing or approach assessments. The middle-source sequence adds a direct view of plume development within the represented seating and overhead-bin geometry. These complementary representations preserve the relationship between source, enclosure and observation.

Height dependence is particularly relevant to selecting assessment coordinates. The 1.1 m records in the front and rear cases remained comparatively clear while the upper station sets experienced widespread attenuation. The middle case introduced a strongly obscured lower-height location adjacent to its source. Thus, a low observation height and a clear route are separate questions: the source location and its local plume also determine the environment at a chosen height. A cabin assessment benefits from following the longitudinal variation at each height and locating the source relative to that profile.

For evacuation wayfinding, the spatial maps identify where the visibility of aisle features and guidance cues should be examined. The reflecting-target estimate represents non-luminous features, while sign recognition also depends on luminance, target dimensions, background conditions and viewing geometry [1,4]. A particular sign can therefore be assessed by combining its visual properties with the smoke distribution along the relevant line of sight. The present

results supply the environmental component of that task and show why its location and observation height deserve explicit specification.

The two descriptive comparison levels also illustrate how a visibility summary depends on the question being asked. At 2.1 m, every case had seven stations below 10 m, while the counts below 5 m differed. A comparison based on the first level emphasises the broad presence of attenuation; the second distinguishes the number of more strongly obscured sampled locations. For an engineering assessment, these summaries are most useful when linked to the visual feature or viewing distance of interest. The station profile and its temporal record retain the context needed to interpret a threshold count.

For firefighting access, reduced visibility changes the ordinary visual cues available during an approach. Research on firefighter locating systems identifies obscuration and unfamiliar surroundings as challenges to orientation [11]. The cabin fields locate where these conditions occur in relation to the source and aisle. Temperature and CO then add different environmental information along the same approach. Retaining the three descriptors at common coordinates supports a more complete description of the conditions confronting a rescue team, including where an optical constraint is spatially extended and where a thermal excursion is more localised.

The spatial findings also inform the placement of observations in comparative fire-protection studies. Upper measurements can describe smoke accumulation, source-adjacent measurements can describe the local plume, and aisle stations can describe the environment encountered along a longitudinal task. Retaining these roles makes it possible to relate a protection measure to the part of the environment it is intended to change. For a guidance assessment, the visual feature and observer position define the relevant viewing path. For an access assessment, the approach coordinates define where thermal, optical and gas records should be considered together. The present comparison supports this task-based selection of observations by showing how the same source produces different patterns in the measured quantities. It also preserves a common layout for comparing changes in the fire environment under a defined assessment design.

Thermal imaging is a further, distinct observation task. Smoke-cell experiments showed that thermal-image contrast depended on camera type and on the temperature difference between a target and its background [12]. Visible-light attenuation can therefore be combined with thermal information when defining an assessment, while each sensing task retains its own relevant response. The calculated visibility field helps locate loss of ordinary visual cues. Camera characteristics and target–background conditions then specify how a thermal imager would be evaluated at those locations. This distinction gives the environmental maps a clear role in planning equipment-oriented rescue studies.

The historical comparison shows that interpretation also depends on how a transient observable is paired with measurements. Holding the 36 saved numerical values, labels and weights fixed

made the L-to-W change directly attributable to the experimental temporal definition. Optical RMSE increased by 15.42%, whereas thermal RMSE changed only slightly and thermal MAE decreased. These outcomes demonstrate that the reported effect of averaging depends on both the observable and the error metric. They also explain why a change between P and W should be understood through the sampling-grid change captured by L.

This temporal perspective complements work on detector response and evolving smoke sources. Detector dynamics introduce their own response times [13], while actual and surrogate smoke can have different early optical histories [9]. Adaptive smoke-generation studies explicitly consider the evolution of the imposed signal [14,15]. In each setting, a numerical comparison benefits from identifying the physical quantity, sampling labels and temporal support. The B707 analysis shows how those choices influence the error reported for one fixed calculation and why optical and thermal records should retain their individual definitions.

The direction of bias depended on the observable and location. The positive pooled thermal bias coexisted with six negative-bias channels, and every optical path had a negative mean bias. CO predictions also exceeded the printed upper uncertainty bounds at all eight unambiguous events. These differences make observable-specific evaluation valuable for fire-protection studies. A model comparison can identify which environmental quantity is overpredicted at which location, while the proposed guidance, detection or intervention measure determines why that discrepancy matters for the assessment.

The choice of error summary further determines which part of this information is retained. Bias preserves the direction of residuals, MAE summarises their absolute magnitude, and RMSE gives greater weight to larger residuals through squaring. Their joint presentation therefore describes different properties of a channel history. In the B707 comparison, the change in thermal MAE alongside a different change in RMSE made this distinction visible. Channel-level results added the spatial distribution that was condensed in the pooled summaries. For interpreting a numerical fire assessment, it is useful to read these measures together with the observable's physical unit and the time support of the comparison. This links an error value to a defined environmental record and to the task for which that record is being interpreted.

The local thermal excursions illustrate how these summaries relate to an environmental time history. A peak value identifies intensity at a selected instant, its timing locates that excursion within the evolving fire, and whole-history error describes deviation across the observation period. Their separation is relevant when a numerical record is used to identify an approach condition or compared with a proposed detection time. The TC23 example retains both magnitude and timing alongside the channel errors. It provides a concrete link between a transient record and the choice of summary used to interpret that record.

Several conditions govern the transfer of these findings. The cabin used an idealised enclosure, prescribed 100 kW sources, fixed-temperature obstacle surfaces and a common ventilation

arrangement over 70 s. Its 0.2 m grid gives a nominal characteristic-fire-diameter-to-cell-width ratio of about 1.9, so spatial convergence is an important next numerical assessment. The source-adjacent middle station also had a different longitudinal offset from the nearest stations in the other cases. These features constrain a general ranking of source positions and direct attention to geometry-specific airflow, heat exchange and consistently defined sampling distances. The cabin evidence is computational; application to a specific aircraft and its evacuation or suppression operations calls for geometry-specific measurements and defined movement or intervention models.

Optical interpretation has additional conditions. The prescribed soot yield, extinction coefficient and reflecting-target factor determine the conversion from concentration to local visibility. A capped local value, a heterogeneous line of sight and the recognisability of a particular target describe different aspects of a visual task. Instantaneous slices and preceding-interval device means also have different temporal support. In the historical comparison, source soot production, wall heat transfer and thermocouple response act alongside the extinction-coefficient difference and gas-probe coordinates. Three approximately 0.08 m recesses contribute to the reported 1.45 m overall experimental height, compared with the main model height of 1.37 m. The report also identifies reduced optical reliability below 80% transmission in the foot convention, equivalent to approximately 48.09% in the metre convention. The early partition study retained cell widths and addressed mesh-interface sensitivity over 0–45 s. Matched measurement responses, refinement and targeted parameter variation would help distinguish these contributions [16,17].

Within these conditions, the results provide a practical basis for selecting observation locations and quantities in further aircraft fire-protection assessments. Evacuation guidance can be examined where the maps show changes in the visibility of aisle features. Firefighter approaches can be defined through the same coordinates while retaining thermal and gas information. Specific suppression measures introduce agent delivery and fire–spray interactions [18], and pressure changes introduce additional cargo-fire behaviour [19]. The present contribution is the spatial and temporal environmental description on which those task-specific comparisons can be built.

Methods

Cabin configuration and prescribed sources

Three FDS 6.11.1 calculations represented a generic single-aisle cabin as a 27.6 × 3.6 × 2.4 m rectangular enclosure (Fig. 2). A uniform 0.2 m mesh, with 138 × 18 × 12 cells, contained 29,808 cells. Thirty paired rows of non-burning seating-bank proxies and two overhead-bin blocks formed 122 obstacles. Source centres were at x = 3.8, 13.8 or 23.8 m and y = 1.8 m. Geometry, material assumptions and ventilation were common to all cases, providing a common setting for comparing source positions.

Seat-row origins were $x_n = 2.0 + 0.8n$ m for n = 0,…,29. Left and right banks occupied y = 0.2–1.4 and 2.2–3.4 m, leaving a 0.8 m central aisle. Each base extended from x_n to $x_n + 0.4$ m and z = 0.4–0.6 m; each back extended from $x_n + 0.4$ to $x_n + 0.6$ m and z = 0.6–1.2 m. Overhead bins occupied x = 2.0–25.6 m and z = 2.0–2.4 m, at y = 0–1.0 and 2.6–3.6 m.

Each floor source occupied 0.8 × 0.4 m. A heat release rate per unit area of 312.5 kW m^{-2} gave a nominal 100 kW plateau. The source multiplier was zero through 10 s, rose linearly to one at 15 s and remained there to 70 s. The propane surrogate used a heat of combustion of 46,400 kJ kg^{-1}, soot yield 0.05, CO yield 0.01 and radiative fraction 0.35. Air was initially quiescent at 20 °C, and enclosure, seating and bin surfaces were held at 20 °C.

The front supply patch lay at x = 0, y = 1.4–2.2 m and z = 0.4–1.6 m. Its flow into the domain rose linearly from zero to 0.4 m^3 s^{-1} over 0–2 s. The rear OPEN patch lay at x = 27.6 m, y = 1.4–2.2 m and z = 0–1.8 m and communicated with ambient air. Each calculation used one MPI process and two OpenMP threads and completed 70 s.

Cabin field extraction and optical quantities

Native float slices supplied temperature and soot mass concentration on the nodal longitudinal plane y = 1.8 m and cell-centred horizontal planes z = 1.7 and 2.1 m. Point devices at y = 1.9 m sampled seven longitudinal stations, x = 2.1, 6.1, 10.1, 13.9, 18.1, 22.1 and 26.1 m, at z = 1.1, 1.7 and 2.1 m. Devices recorded temperature, visibility and CO. The CO conversion factor of 10^6 in the input produced output in ppm.

Extinction was calculated as $K = K_m \rho_s$, where ρ_s is saved soot mass concentration in kg m^{-3} and $K_m = 8700$ m^2 kg^{-1}. Reflecting-target visibility was S = min(30 m, 3/K), with S = 30 m at K = 0 [2]. The cap therefore represents an underlying estimate of at least 30 m. The historical optical devices used the reference-length transmission definition given below.

The 36 saved slice frames retained their actual times. The frame nearest 20 s was at 20.02000046 s; frames at 40, 60 and 70 s used exact saved labels. Initialized obstacle masks removed solids without smoothing the remaining fields. Longitudinal space–time maps used the saved z = 1.6 m node on y = 1.8 m. Smokeview rendered the middle-case soot-density and heat-release fields in a fixed view; Python produced the quantitative maps directly from the float slices.

Each device file contained an initial record and 140 subsequent means over preceding output intervals, nominally spaced by 0.5 s. Extrema and station counts used those means after the initial record over 0–70 s. The 5 and 10 m levels were descriptive comparison levels. Temperature, CO and visibility extrema were calculated independently. Instantaneous slice values and recorded interval means were summarised separately.

Independent historical cargo calculation

The historical reference was the baseline B707 cargo experiment in FAA report DOT/FAA/AR-07/27 [10]. We used its archived experimental CSV at firemodels/exp revision e5de6811036d252b4f9085866f08da66efdda7d3 [20] and the corrected B707 Test 1 input at firemodels/fds revision 72b2205068d989350eb95743070c583232fa6654 [21]. These fixed files specify the full source ramp, nominal sensor coordinates, materials and stepped side-block geometry. The analysis covered 0–180 s of the 0–300 s experimental record. Baseline thermocouple rises are ensemble means from 15 repeated tests; gas-event means are based on five repetitions.

FDS build FDS-6.11.1-0-gff928db-release was used [2]. The domain was x = −1.59 to 1.59 m, y = 0–6.73 m and z = 0–1.37 m. The model represented the main compartment volume with stepped side obstacles. The prescribed side-block profile ended at z = 1.3281 m. FDS mapped these blocks to the computational cells.

The 739,200-cell reference arrangement was repartitioned from five to eight meshes by splitting the fine region at y = 3.43–4.03 m into four x blocks of 40, 50, 40 and 30 cells and retaining the four coarse regions. Cell widths remained approximately 20 mm near the source and 40 mm outside. The original and repartitioned calculations had identical initialized Boolean solid masks, a discrete gas volume of 24.755126978 m^3 and 25 exposed source faces totalling 0.0099375 m^2. The eight-mesh calculation used eight MPI processes and one OpenMP thread per process to 180 s.

The input specified SVLES; the initialized model used Deardorff eddy viscosity with coefficient 0.10, WALE surface treatment with coefficient 0.60, and turbulent Prandtl and Schmidt numbers of 0.50. The pressure solver used the FFT formulation with at most ten iterations. Initial temperature and pressure were 20 °C and 101,325 Pa. Radiation used 104 control angles, a time-step increment of three and an angle increment of five.

Wall and ceiling FGLASSE layers had density 1694 kg m^{-3}, heat capacity 1.0 kJ kg^{-1} K^{-1}, conductivity 0.25 W m^{-1} K^{-1} and emissivity 0.90. Thicknesses were 0.30 m for the walls and 0.00058 m for the ceiling, with exposed backing. The source upper face used FIRE; its other faces used BOX with CARDBOARD properties: density 200 kg m^{-3}, heat capacity 1.0 kJ kg^{-1} K^{-1}, conductivity 0.10 W m^{-1} K^{-1}, emissivity 0.80 and thickness 0.10 m. Two nominal 1.40 × 0.04 m OPEN patches at y = 0 and 6.73 m, x = −0.70 to 0.70 m and z = 0–0.04 m provided ambient exchange without imposed mechanical flow.

The prescribed Mixed Polymers fuel had C/H/O/N coefficients 1/3.8/0.3/0.4, specific heat 1.5 kJ kg^{-1} K^{-1} and heat of combustion 18,500 kJ kg^{-1}. CO and soot yields were 0.095 and 0.126 kg kg^{-1}, and radiative fraction was 0.55. The nominal source block occupied x = 0.03–0.13 m, y = 3.68–3.78 m and z = 0–0.02 m. Its upper face supplied a base mass flux of 0.016 kg m^{-2} s^{-1}

multiplied by the retained 38-node piecewise-linear ramp. The terminal ramp node at 350 s remained part of the input definition; calculation and comparison ended at 180 s.

Historical observations and reference-length conversion

The principal comparison comprised TC1–TC40 and LT_Fwd, LT_Mid, LT_Aft, LT_High, LT_Med and LT_Low. THERMOCOUPLE devices with RELATIVE enabled supplied temperature rises in K, including convective and radiative response. Default thermocouple properties were a 1 mm bead, emissivity 0.85 and density 8700 kg m^{-3}; the Type K heat-capacity relation increased linearly from 0.4515 kJ kg^{-1} K^{-1} at 20 °C to 0.601 kJ kg^{-1} K^{-1} at 1200 °C.

FDS TRANSMISSION reported transmission percentage normalised to a 1 m reference path, denoted T_m and written as %/m. Transmission at a 0.3048 m reference length was obtained using Eq. (1). Experimental values slightly above 100 were retained. Residuals are percentage-point differences within the specified reference-length convention.

$$T_{0.3048} = 100\left(\frac{T_m}{100}\right)^{0.3048} \tag{1}$$

For the historical event comparison, simulation values were interpolated in the metre convention before applying Eq. (1). This ordering retained the nonlinear reference-length transformation. The initialized soot mass extinction coefficient was 8700 m² kg^{-1}; the older calculation in the FAA report used 7400 m² kg^{-1}. Both values were retained as properties of their respective calculations.

Gas volume fractions were converted once to ppm by multiplication by 10^6. CO_2 was evaluated as a rise above its initial baseline, while CO had zero initial background. Saved gas means were linearly interpolated to 60, 120 and 180 s before conversion to ppm and comparison with the report's event means and intervals. Mid and Aft probes initialized at approximately z = 1.36961 m, compared with 1.42 m in the report. The TC36 gas probe was at (−1.32, 6.57, 1.33) m; reported longitudinal position and height were 6.52 and 1.35 m. These differences remained part of the historical event comparison.

Temporal pairing and error analysis

The historical device file contained an initial value at 0 s and 36 subsequent interval means through 180 s. Native label spacing was 4.99–5.01 s. Let s(c,k) be the stored value for channel c at label τ_k and E(c,t) the piecewise-linear interpolant of the experimental ensemble record. Protocol P interpolated adjacent finite simulation records to the 181 experimental labels t_j = 0,1,…,180 s using Eq. (2).

$$\hat{s}_c^P(t_j) = s_{c,k-1} + (s_{c,k} - s_{c,k-1})\frac{t_j - \tau_{k-1}}{\tau_k - \tau_{k-1}}, \qquad \tau_{k-1} \le t_j \le \tau_k \tag{2}$$

Protocol L paired the same saved simulation means with experimental endpoint values at the 36 nonzero native labels using Eq. (3). It provided the endpoint-value control for W, with the same simulation values, labels, counts and weights.

$$e_{c,k}^{L} = s_{c,k} - E_c(\tau_k), \quad k = 1, \ldots, 36 \tag{3}$$

Protocol W paired each saved value with the experimental mean over its preceding recorded-label interval, as defined in Eq. (4). The piecewise-linear experimental series was integrated exactly by inserting interval endpoints and applying trapezoidal integration across all enclosed knots. The initial record was excluded because it has no preceding interval, giving 36 pairs per channel. Recorded-label windows defined the experimental integration intervals.

$$e_{c,k}^{W} = s_{c,k} - \frac{1}{\Delta\tau_k}\int_{\tau_{k-1}}^{\tau_k} E_c(t)\,dt, \quad \Delta\tau_k = \tau_k - \tau_{k-1} \tag{4}$$

Residuals were simulation minus experiment. RMSE, MAE and bias used equal weights within each comparison, with additional duration-weighted L and W summaries. Errors were pooled separately for thermocouple rise and transmission using Eqs. (5) and (6). P to L changed the sampling grid; L to W changed experimental temporal support at fixed numerical values and labels.

$$RMSE = \sqrt{\frac{1}{N}\sum_{n=1}^{N} {e_n}^2}, \quad MAE = \frac{1}{N}\sum_{n=1}^{N} |e_n|, \quad bias = \frac{1}{N}\sum_{n=1}^{N} e_n \tag{5}$$

$$RMSE_{pool} = \sqrt{\frac{\sum_{c=1}^{C}\sum_{n=1}^{N_c} w_{c,n}{e_{c,n}}^2}{\sum_{c=1}^{C}\sum_{n=1}^{N_c} w_{c,n}}}, \qquad w_{c,n} = 1 \text{ or } \Delta\tau_n \tag{6}$$

The analysis used finite values and strictly increasing native labels. Interpolation was confined to the common observation range and to adjacent finite records separated by at most 12.5 s. Interpolation, interval integration and error summaries were implemented in Python with NumPy and the standard library.

The FAA report provides test-specific uncertainty information [10]. The reported thermal 95% ranges combine experimental variability with a 0.5 K drift component. The 19 optical events were those explicitly tabulated in the report. All 18 printed gas entries were retained for source interpretation; two inconsistent TC36 entries at 60 s were excluded from interval judgements. Printed total 95% half-widths were used directly.

Partition sensitivity compared the eight-mesh calculation with a separate five-mesh calculation over their common 0–45 s interval. All 46 principal channels and heat release were interpolated to an integer-second grid. Differences were eight-mesh minus five-mesh values, with unchanged spatial resolution.

Funding

This research was supported by the Science and Technology Program of the National Fire and Rescue Administration of China (Grant No. 2026XFCX07), the Young Faculty Research Start-up Fund of the Civil Aviation Management Institute of China (Grant No. 25QN03), and the Open Fund of the Key Laboratory of UAV Emergency Rescue Technology, Ministry of Emergency Management (Grant No. UERT202605).

Competing interests

The authors declare no competing interests.

Data availability

The historical FAA Boeing 707 cargo-compartment experimental dataset analysed in this study (TestCase1_FAA_EXPDATA.csv) is publicly available in the firemodels/exp repository at the fixed revision linked here: https://github.com/firemodels/exp/blob/e5de6811036d252b4f9085866f08da66efdda7d3/FAA_Cargo_Compartments/TestCase1_FAA_EXPDATA.csv (Ref. [20]).

Code availability

FDS 6.11.1 and the reference cargo input are available through the cited NIST documentation and firemodels repository [2,21]. The postprocessing used Python, NumPy and the standard library. Requests for the cabin input files and analysis scripts should be directed to the corresponding author.

References

1. Rasmussen, P. G., Chesterfield, B. P. & Lowrey, D. L. *Readability of Self-Illuminated Signs Obscured by Black Fuel-Fire Smoke.* FAA-AM-80-13, Federal Aviation Administration (1980). https://www.govinfo.gov/content/pkg/GOVPUB-TD4_200-PURL-LPS81960/pdf/GOVPUB-TD4_200-PURL-LPS81960.pdf

2. McGrattan, K. et al. *Fire Dynamics Simulator User's Guide.* NIST Special Publication 1019, 6th edn, revision FDS-6.11.1-0-gff928db (2026). https://doi.org/10.6028/NIST.SP.1019

3. Mulholland, G. W. & Croarkin, C. Specific extinction co

efficient of flame generated smoke. *Fire Mater.* **24,** 227–230 (2000). https://doi.org/10.1002/1099-1018(200009/10)24:5%3C227::AID-FAM742%3E3.0.CO;2-9

4. Börger, K., Belt, A., Schultze, T. & Arnold, L. Remote sensing of the light-obscuring smoke properties in real-scale fires using a photometric measurement method. *Fire Technol.* **60,** 19–45 (2024). https://doi.org/10.1007/s10694-023-01470-z

5. Blake, D. & Suo-Anttila, J. Aircraft cargo compartment fire detection and smoke transport modeling. *Fire Saf. J.* **43,** 576–582 (2008). https://doi.org/10.1016/j.firesaf.2008.01.003

6. Papa, R., Andrade, C. R., Zaparoli, E. L. & de C. Santos, L. C. CFD analysis of smoke transport inside an aircraft cargo compartment. *J. Braz. Soc. Mech. Sci. Eng.* **38,** 327–334 (2016). https://doi.org/10.1007/s40430-015-0307-7

7. Lu, K. H., Mao, S. H., Wang, J. & Lu, S. Numerical simulation of the ventilation effect on fire characteristics and detections in an aircraft cargo compartment. *Appl. Therm. Eng.* **124,** 1441–1446 (2017). https://doi.org/10.1016/j.applthermaleng.2017.06.128

8. Chen, X., Ouyang, J. & Yang, J. Optimal detector placement for fire smoke detection in ventilated aircraft cargo compartment. *Fire Technol.* **58,** 2251–2281 (2022). https://doi.org/10.1007/s10694-022-01259-6

9. Chen, X., Shao, Z. & Yang, J. Comparison between actual and simulated smoke for smoke detection certification in aircraft cargo compartments using the CFD method. *Fire Technol.* **56,** 469–488 (2020). https://doi.org/10.1007/s10694-019-00887-9

10. Suo-Anttila, J., Gill, W., Luketa-Hanlin, A. & Gallegos, C. *Cargo Compartment Smoke Transport Computational Fluid Dynamics Code Validation.* DOT/FAA/AR-07/27, Federal Aviation Administration (2007). https://www.fire.tc.faa.gov/pdf/07-27.pdf

11. Putorti, A. D., Jr. et al. *Structural and Electromagnetic Scenarios for Firefighter Locator Tracking Systems.* NIST Technical Note 1713 (2011). https://www.nist.gov/publications/structural-and-electromagnetic-scenarios-firefighter-locator-tracking-systems

12. Kim, S. C. & Hamins, A. Bench-scale test facility for evaluating the performance of thermal imagers for fire service applications. *J. Fire Sci.* **36,** 97–110 (2018). https://doi.org/10.1177/0734904117753351

13. Cui, H. et al. Study on response time hysteresis model of smoke detectors in aircraft cargo compartment. *Fire* **7,** 317 (2024). https://doi.org/10.3390/fire7090317

14. Chen, X. et al. Design of an unsteady smoke simulation system for the airworthiness verification of smoke detection in aircraft cargo compartments based on the adaptive flow control method. *Aerospace* **12,** 148 (2025). https://doi.org/10.3390/aerospace12020148

15. Chen, X. et al. Model-free adaptive predictive control for dynamic surrogate smoke simulation in aircraft cargo fire detection testing. *Fire* **9,** 361 (2026). https://doi.org/10.3390/fire9090361

16. McGrattan, K. & Toman, B. Quantifying the predictive uncertainty of complex numerical models. *Metrologia* **48,** 173–180 (2011). https://doi.org/10.1088/0026-1394/48/3/011

17. Paudel, D. & Hostikka, S. Propagation of model uncertainty in the stochastic simulations of a compartment fire. *Fire Technol.* **55,** 2027–2054 (2019). https://doi.org/10.1007/s10694-019-00841-9

18. Zhu, P. et al. Numerical study on fire suppression by water mist in aircraft cargo compartments: effects of spray pattern, droplet size, and nozzle layout. *Fire* **7,** 481 (2024). https://doi.org/10.3390/fire7120481

19. Li, M., Chen, Y., Zhao, Y. & Wang, J. Flashover in aircraft cargo compartment at different pressures: experimental and modeling study. *Fire* **6,** 415 (2023). https://doi.org/10.3390/fire6110415

20. Firemodels. FAA cargo compartments experimental data, TestCase1 FAA EXPDATA. *GitHub* (2026). https://github.com/firemodels/exp/blob/e5de6811036d252b4f9085866f08da66efdda7d3/FAA_Cargo_Compartments/TestCase1_FAA_EXPDATA.csv (accessed 23 October 2026).

21. Firemodels. FAA B707 Test 1 reference input. *GitHub* (2026). https://github.com/firemodels/fds/blob/72b2205068d989350eb95743070c583232fa6654/Validation/FAA_Cargo_Compartments/FDS_Input_Files/FAA_B707_Test_1.fds (accessed 23 October 2026).